Energy & Environmental Science

ROYAL SOCIETY OF CHEMISTRY

PAPER

View Article Online
View Journal

Check for updates

Cite this: DOI: 10.1039/d5ee00217f

Ultra-uniform interfacial matrix *via* high-temperature thermal shock for long-cycle stability cathodes of sodium-ion batteries†

Zekun Li,[a] Pengfei Huang,[ac] Jinfeng Zhang,[a] Zhaoxin Guo,[a] Zhedong Liu,[a] Li Chen,[a] Jingchao Zhang,[a] Jiawei Luo,[a] Xiansen Tao,[e] Zhikai Miao,[a] Haoran Jiang,[a] Chunying Wang,[a] Xinran Ye,[a] Xiaona Wu,[b] Wei-Di Liu,[d] Rui Liu,[b] Yanan Chen*[a] and Wenbin Hu*[a]

Received 13th January 2025,
Accepted 6th February 2025

DOI: 10.1039/d5ee00217f

rsc.li/ees

$NaNi_{1/3}Fe_{1/3}Mn_{1/3}O_2$ (NFM333) is a promising cobalt-free, high-capacity cathode material for sodium-ion batteries, but suffers from poor cycling stability when prepared by the conventional tube furnace method due to electroactive metal migration, leading to a passive surface layer. To address this challenge, a high-temperature shock (HTS) method was employed. Compared to the tube furnace method, HTS offers a rapid heating process that contributes to a more compact and ultra-uniform $NaCaPO_4$ (NCP) coating, leading to enhanced structural integrity and coating quality. The HTS method first enables the formation of a compact and ultra-uniform NCP coating, which prevents nickel migration more effectively compared to tube furnace-prepared NFM333 (Tu-NFM333). By preventing nickel migration, the surface residual alkalinity is reduced, enhancing air stability and improving electrochemical performance. As a result, HTS-treated NFM333 demonstrated 80% capacity retention after 1000 cycles at a 1C rate, while a pouch cell retained 70% capacity after 700 cycles. The stabilization of NFM333 through HTS highlights a promising approach for developing durable sodium-ion batteries.

Broader context

The cobalt-free cathode material $NaNi_{1/3}Fe_{1/3}Mn_{1/3}O_2$ (NFM333) emerges as a promising candidate for sodium-ion batteries owing to its high capacity and significant industrial potential. However, the conventional tube furnace synthesis method often results in poor cycling stability, as prolonged heating can lead to nickel precipitation, which diminishes the capacity of material. To mitigate this issue, a high-temperature shock (HTS) method was utilized for surface modification using $NaCaPO_4$, resulting in a dense and highly uniform coating that effectively suppresses nickel migration and enhances the material's structural integrity. Moreover, this uniform coating reduces surface residual alkalinity, thereby enhancing both air stability and electrochemical performance. After HTS treatment, NFM333 retained 80% of its capacity after 1000 cycles at a 1C rate, while a pouch cell maintained 70% capacity retention after 700 cycles, demonstrating the material's excellent cycling stability.

Introduction

Sodium-ion batteries (SIBs) are a promising option for large-scale energy storage due to high earth-abundance of sodium.[1–3] Layered sodium transition metal oxides (Na_xTMO_2) have attracted extensive research interest for high capacity and operating voltage. Generally, Na_xTMO_2 ($0 < x \leq 1$, TM: transition metal) is composed of O3 and P2 phases. The O3–Na_xTMO_2, with a high sodium content, stands out due to superior reversible and reliable capacity among sodium-ion electrodes.[4–6]

Among various O3–Na_xTMO_2, cobalt-free cathode material $NaNi_{1/3}Fe_{1/3}Mn_{1/3}O_2$ is cost-effective, eco-friendly, and structurally stable.[7–10] Nickel plays a key role by facilitating electron transfer, thus enhancing capacity. However, nickel solubility in

---

[a] School of Materials Science and Engineering, Tianjin University, Tianjin, 300072, China. E-mail: yananchen@tju.edu.cn, wbhu@tju.edu.cn
[b] School of Materials Science and Engineering, Shandong University of Science and Technology, Qingdao, 266590, China
[c] Key Laboratory of Coal Processing and Efficient Utilization of Ministry of Education, China University of Mining and Technology, Xuzhou, 221116, Jiangsu, China
[d] School of Chemistry and Physics (Faculty of Science), ARC Research Hub in Zero-emission Power Generation for Carbon Neutrality, and Centre for Materials Science, Queensland University of Technology, Brisbane, QLD 4000, Australia
[e] School of Chemistry, Chemical Engineering and Materials, Jining University, Qufu, 273155, China

† Electronic supplementary information (ESI) available. See DOI: https://doi.org/10.1039/d5ee00217f

the O3 phase is strongly constrained by calcination temperature and time, leading to NiO precipitates and degraded performance.[11–15] An ultra-uniform coating technique can create a consistent layer on cathode materials, avoiding cathode–electrolyte interface degradation. This coating introduces a protective layer that reduces side reactions, enhances stability, and improves pathways for sodium-ion and electron transport. Furthermore, this scalable method offers a practical approach for developing next-generation sodium-ion batteries, with extended lifespan and improved efficiency.[16–18]

Plastic crystals, discovered in 1935, are transitional states with high ionic conductivity between crystalline materials and liquids. Na_3PO_4, a sodium-based plastic crystal, changes from low-symmetry α-Na_3PO_4 to high-symmetry cubic γ-Na_3PO_4 at about 600 K, improving ionic conductivity.[19] γ-Na_3PO_4 can be stabilized at room temperature by substituting sodium with elements like Mg, Al, and Ca. Hu and Sun showed that coating sodium-ion cathodes with sodium-containing plastic crystals removes excess sodium, protects against erosion, and enhances sodium ion transport.[20–24] These enhancements collectively boost the electrochemical performance of the batteries. However, the γ-Na_3PO_4 is unstable at room temperature. Consistently performing across a broad temperature range while ensuring an even coating on the cathode material remains a significant challenge.

In this work, we employed a high-temperature shock technique to synthesize NFM333. This approach results in reduced surface alkali, and enhanced stability in air.[25–30] To further enhance the electrochemical performance, a plastic-crystal coating was applied using HTS. It is found that HTS can effectively prevent nickel separation and contribute to phase purification of the coating layer, compared with tube furnace (tube) synthesis. Rapid quenching in HTS also preserves the γ-phase coating and boosts the ion conductivity. In battery performance tests, $NaCaPO_4$-coated $NaNi_{1/3}Fe_{1/3}Mn_{1/3}O_2$ composites synthesized by high-temperature shock (denoted as HT-NCP@333) underwent 1000 charge–discharge cycles at a 1C rate, achieving a capacity retention of 80%. This capacity retention significantly outperforms conventionally synthesized materials, demonstrating superiority of HTS in stabilizing battery performance. After 700 cycles at a 1C rate, the HT-NCP@333//HC pouch cell also maintained a 70% capacity retention, confirming its commercial viability and durability.

Results and discussion

Synthesis and structural characterization

Fig. 1 clearly illustrates the synthesis process of $NaCaPO_4$ (NCP)-coated NFM333 (NCP@333), which incorporates HTS and tube methods. The temperature distribution on the nickel foil surface during the HTS process demonstrates uniform and stable temperature control (Fig. S4(a), ESI†). The spherical NFM333 precursor, synthesized *via* co-precipitation with a D50 (D50 is the particle size at which half of the particles are larger, and half are smaller) of ∼6 microns, is used for HTS and tube thermal treatments (Fig. S1 and S2, and Table S1, ESI†). The heating and cooling rates are increased to reach the target temperature within 2 s, and the temperature curve is shown in Fig. S4(b) (ESI†). The process begins with pre-calcination at around 500 °C for 60 seconds to remove organic components, followed by final calcination at ∼835 °C for 60 seconds,

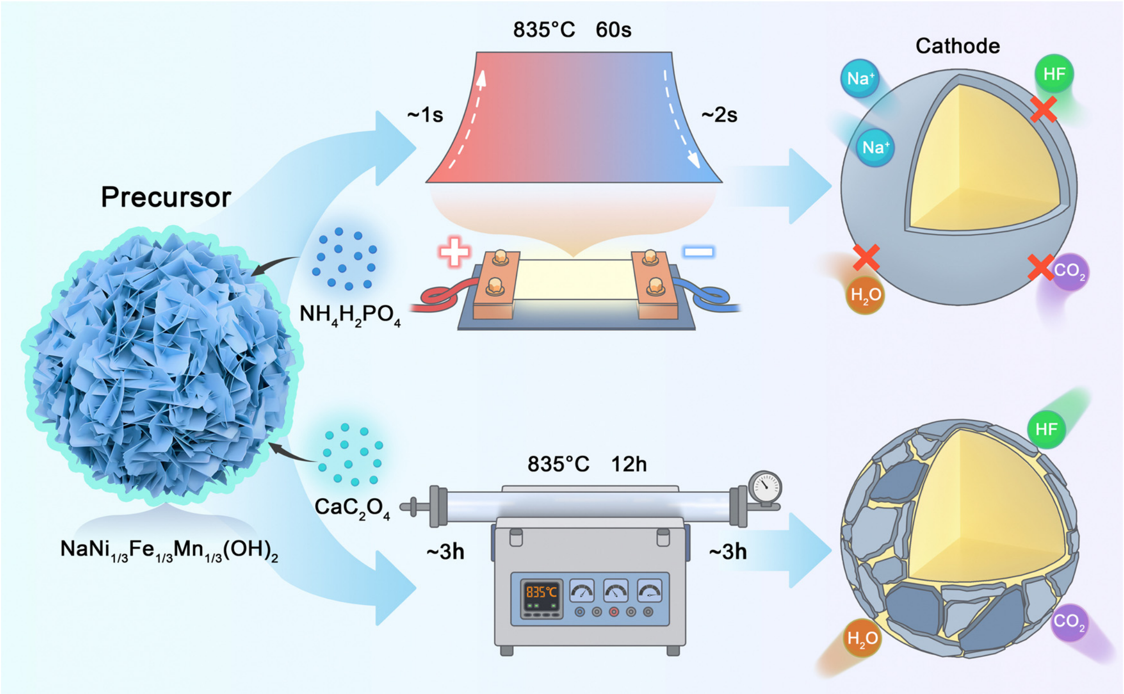

Fig. 1 Schematic illustration of the formation process of HT-NCP@333 and Tu-NCP@333.

forming HT-NCP@333 (Fig. 1). Despite the rapid synthesis with minimal thermal ramping and cooling periods, the products maintain a fine crystalline structure. The HT-NCP@333 synthesized *via* the HTS method features a uniform and single-phase plastic crystal coating. After calcination, a green layer (identified as Na_3MnO_4) appeared on the crucible surface used for uncoated samples. Whereas no such byproduct was detected on the crucible surface used for NCP-coated counterparts (Fig. S8, ESI†). This phenomenon aligns well with the XRD analyses presented in Fig. S9 (ESI†) and Fig. 2, confirming that NCP coating can effectively suppress the formation of surface impurities (Na_3MnO_4) during calcination. The high-angle annular dark field scanning transmission electron microscopy (HAADF-STEM) image of HT-NCP@333, reveals a highly crystalline structure. The HAADF image of the HT-NCP@333 cathode material demonstrates high crystallinity, structure integrity and the potential for high electrochemical performance (Fig. S3, ESI†). In contrast, the tube furnace synthesized NCP@333 (Tu-NCP@333) presents a complex surface structure, comprising the coating layer, unstable NiO rock salt phases and residual alkalis resulting from interactions with atmospheric water or CO_2 (Fig. 1). The Tu-NCP@333 was synthesized using a tube and HTS methods. X-ray diffraction (XRD) refinement shows that both HT-NCP@333 and Tu-NCP@333 exhibit a well-defined layered structure (Fig. S9, ESI†). In contrast, the HTS method results in a purer product with fewer impurities as evidenced by XRD patterns and improved refinement parameters (R_w = 2.13%, R_{wp} = 1.08%, χ^2 = 1.27). This demonstrates superiority of the HTS method for synthesizing high-purity NFM333 layer oxides. The crystallographic parameters are

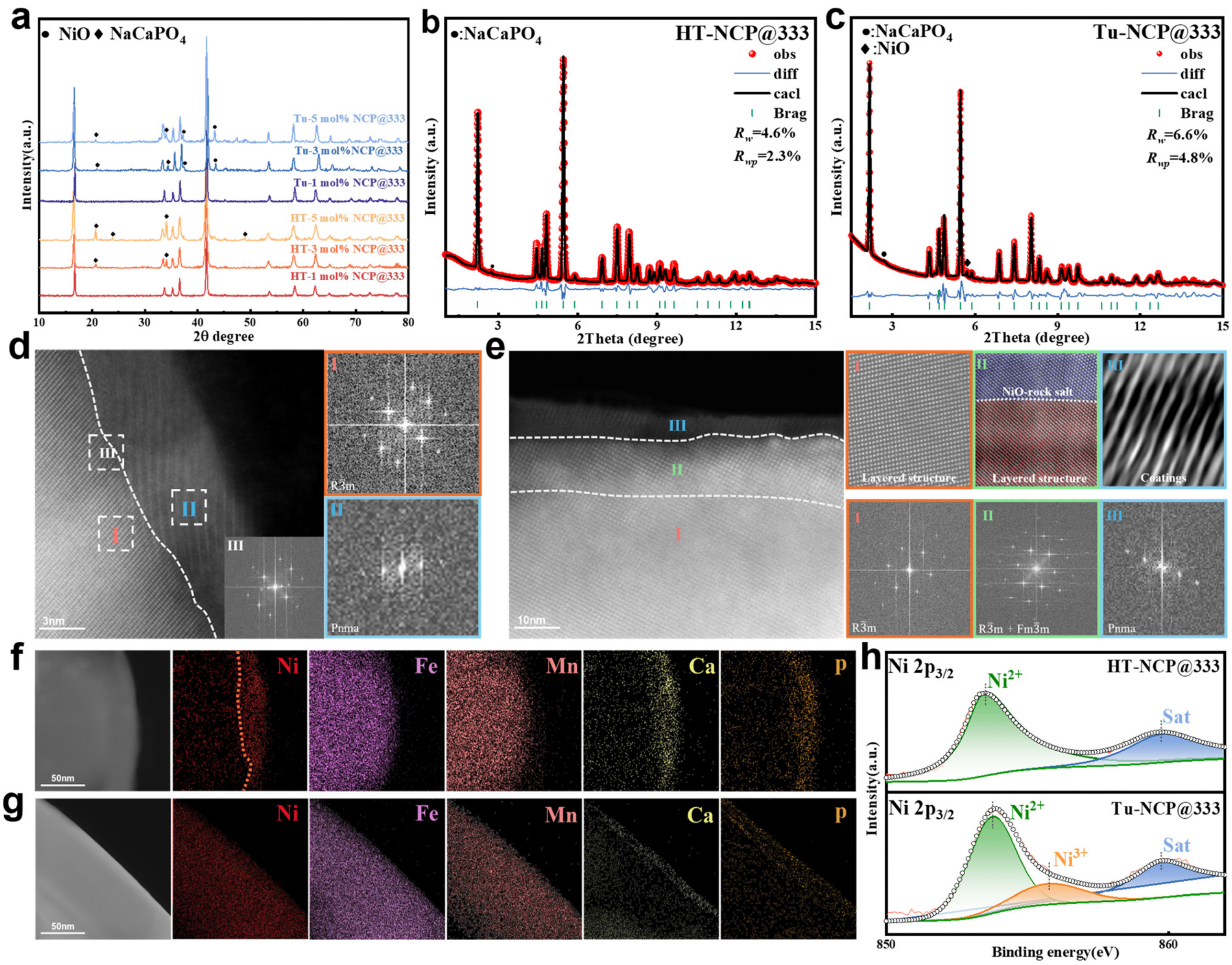

Fig. 2 Structural comparison between HT-NCP@333 and Tu-NCP@333. (a) XRD patterns for 0.5, 1, 3, and 5 mol% NCP@333 synthesized by HTS and tube. (b) and (c) Refined synchrotron X-ray diffraction pattern of the HT-NCP@333 and Tu-NCP@333 samples. (c) HAADF-STEM of HT-NCP@333 surface showing an architecture consisting of Region I and II, separated by the dashed lines. (d) HAADF-STEM of HT-NCP@333 surface showing an architecture consisting of regions I, II and III, corresponding reduced fast Fourier transform (FFT) image of the selected area (orange and blue squares). (e) HAADF-STEM of Tu-NCP@333, inverse fast Fourier transformed (IFFT) images and corresponding FFT patterns of selected regions I, II and III (orange, green and blue squares); atomic column localization of the layered structure phase and the NiO rock-salt phase, with region II separated by orange dashed lines. (f) and (g) STEM images and the corresponding EDS element maps of Ni, Fe, Mn, Ca and P for HT-NCP@333 and Tu-NCP@333. (h) *Ex situ* Ni 2p XPS spectra of HT-NCP@333 and Tu-NCP@333.

listed in Tables S3 and S4 (ESI†). The scanning electron microscopy (SEM) images show that HTS-synthesized NFM particles (HT-333) have a rough but uniform surface composed of primary particle aggregates. In contrast, tube-synthesized particles exhibit surface defects due to prolonged thermal treatment, as highlighted by the blue annotations (Fig. S5, ESI†). Ca 2p X-ray photoelectron spectroscopy (XPS) analysis shows that calcium is integrated into the structure of Tu-NCP@333 and HT-NCP@333 (Fig. S29, ESI†). However, excessive calcium doping has led to the penetration of calcium ions into the interior of NCP@333. Although this doping enhances the electrochemical performance of O3 cathode materials, the mechanism lying behind this improvement remains unclear.[31]

Density functional theory (DFT) was used to study the effects of calcium doping on the electronic structure and phase transition of Na–Ni–Mn–O oxide materials. Fig. S6 (ESI†) shows the projected density of states (PDOS) and the electron localization function (ELF) of both Ca-doped and undoped $NaNi_{1/3}Fe_{1/3}Mn_{1/3}O_2$. Ca-doping increases the density of electronic states near the Fermi level, suggesting improved electrical conductivity and electron mobility.[32] Moreover, significant alterations in d-orbital contributed by iron, nickel, and manganese suggesting a reallocation of charge, enhanced charge conductivity. Ca-doping reduces the energy levels of the cathode, prompts electron localization due to additional electrons from calcium, and improves catalytic and electrochemical functions. Broadly, calcium doping augments electron localization, structural robustness, and redox reversibility, underscoring its importance in refining material properties for targeted technologies. XPS and Fourier transform infrared (FTIR) spectroscopy results reveal that Tu-NCP@333 exhibits more surface residual alkalis, indicated by stronger carbonate presence and potential CO_2 generation. In contrast, the HT-NCP@333 has fewer residual alkalis, indicating that HTS is a more appropriate approach for high surface purity and reactivity (Fig. S7 and S10, ESI†).

Fig. 2(a) shows the X-ray diffraction (XRD) patterns of HT-333 and Tu-333 coated with 1, 3, and 5 mol% NCP, respectively. The patterns reveal pronounced peaks of the NCP phase, which become sharper and more intense with increasing coating content. With increasing NCP coating content, increased Ca doping in the bulk phase shifts the diffraction peaks to lower angles due to further lattice expansion. Notably, Tu-NCP@333 demonstrates additional characteristic peaks of the NiO rock salt phase, whose peak intensity becomes more pronounced with increasing coating amount. In contrast, the HTS method effectively preserves the original O3 structure of HT-NCP@333 across all coating amounts without introducing impurities, demonstrating its superiority in preserving stability and refraining impurity formation during synthesis. Synchrotron XRD patterns in Fig. 2(b) and (c) confirm these findings. The HT-NCP@333, shown in Fig. 2(b), exhibits no NiO impurities and better crystallographic quality. Refined parameters for the HT-NCP@333 (R_w = 4.6%, R_{wp} = 2.3%) are lower than Tu-NCP@333, suggesting improved fitting quality and phase purity. The Rietveld refinement results are detailed in Tables S5 and S6 (ESI†). The characterization results revealed a c-lattice parameter of 15.633 Å for the Tu-NCP@333. In contrast, the c-lattice parameter for the HT-NCP@333 sample is slightly longer at 16.026 Å. This increase suggests enhanced sodium ion transport efficiency in the HT-NCP@333, illustrating the superiority of the HTS method to produce high-purity NFM333 layered oxide materials with NCP coatings. Fig. 2(d) and (e) shows HAADF-STEM images of HT-NCP@333 and Tu-NCP@333 cathode microparticles, respectively. In Fig. 2(d), NCP nanoparticles are tightly packed without gaps from the substrate, marked by a dotted line. The NCP film is approximately 8 nm thick. The insets on the right show their fast Fourier transform (FFT) analysis, revealing a uniform NCP coating layer formed through HTS synthesis, which prevents the formation of NiO rock-salt structures. Fig. 2(e) highlights three distinct textured areas, labeled as I, II, and III, representing different layers in Tu-NCP@333. The NCP coating is dispersed over the material surface in region III. Additionally, the surface of the NFM333 cathode materials shows significant changes, transitioning from a layered $R\bar{3}m$ structure to an $Fm\bar{3}m$ space group rock-salt structure, usually associated with sodium deficiency. A contaminant phase of rock-salt NiO is visible on the surface, marked by a crimson border in the upper right sub-panel I and II, suggesting structural irregularities that might affect the material performance. To demonstrate this point, an innovative AI-assisted technique for segmenting phases atom-by-atom was utilized to automatically identify the NiO rock salt phase within the O3 matrix from super-resolution images.[33] This approach automatically segmented phases at an atomic level. Fig. 2(e) of section II, shows a map illustrating the clearly defined NiO rock salt phase on the particle surface. Moreover, the lower right sub-panel shows additional fast Fourier transform (FFT) analysis, providing intricate insights into atomic spacing and orientation. These observations are imperative for assessing the material phase constitution and the existence of diverse crystalline configurations within the particles. Elemental maps of the coating samples were performed using energy-dispersive spectroscopy (EDS), which confirms a higher concentration of Ni on the surface of Tu-NCP@333. This suggests that Ni segregates from the material matrix to the surface. Conversely, in the HT-NCP@333, Ni is uniformly distributed (Fig. 2(f) and (g)). Additionally, the results clearly demonstrate the successful deposition of the plastic crystal-NCP on the surface of NFM333. Transmission electron microscopy (TEM) images reveal detailed structural characteristics of Tu-NCP@333, showing a rock-salt NiO surface alongside an NCP coating (Fig. S11(a), ESI†). High-resolution TEM (HRTEM) analysis identifies distinct lattice fringes with spacings of approximately 2.41 Å and 2.62 Å, corresponding to the crystal planes of NiO and NCP, respectively. In contrast, the HT-NCP@333 shows a consistent NCP coating without impurities formation, indicating a more stable crystal structure (Fig. S11(b), ESI†). XPS analysis reveals that the HTS synthesized material mainly contains Ni^{2+}, whereas the Tu-NCP@333 has a trace amount of Ni^{3+} (Fig. 2(h)). In the process of material synthesis, inconsistent distribution of nickel on the Tu-NCP@333 surface is caused by segregation. High-temperature shock provides significant advantages over traditional tube furnace calcination by producing O3 structured materials with enhanced thermodynamic stability. The rock salt phase on the outer surface impedes the transport of sodium ions due to its poor ionic conductivity.[34]

To examine NiO structure precipitates, Fig. S12(a) (ESI†) compares the XRD patterns of HT-333 and Tu-333, with 5 mol% calcium doping and 5 mol% Na_3PO_4 coating. Calcium doping did not cause Ni segregation in either method. However, NiO precipitation was observed in Na_3PO_4-coated materials created *via* the tube method, compared with HT-Na_3PO_4@333. This is because sodium in the coating layer reduces the sodium needed for synthesis, leading to sodium-deficient materials. Fig. S12(b) (ESI†) confirms the phase formation in sodium-deficient NFM333 materials of both HT-333 and Tu-333 with a Na content of 0.95 mol%. NiO precipitation was detected only in materials synthesized *via* the tube method. Fig. S13 (ESI†) compares the XRD patterns of 5 mol% NCP@333 during different holding times. It can be seen that NiO is primarily formed due to extended high-temperature exposure rather than rapid cooling. This clarifies the occurrence of NiO impurities in materials produced by the tube method. XRD patterns of 5 mol% NCP@333 during different dwelling times in the pipe process show an increase in the NiO rock-salt phase with longer holding periods (Fig. S14, ESI†). This suggests that extended dwelling time is the main reason for Ni segregation in the material. Fig. S15 (ESI†) compares the electrochemical performance of HT-NCP@333 and Tu-NCP@333 without dwelling. HT-NCP@333 demonstrates better performance due to accelerated thermodynamics, enhanced stability and reduced surface alkali residues. Conversely, Tu-NCP@333 without dwell exhibits inferior performance, and hindered evaluations. To further validate the applicability of HTS, $Na_{3-3x}Al_xPO_4$@333, $NaMgPO_4$@333, and $NaTi_2(PO_4)_3$@333 were synthesized using both the HTS and tube methods. Materials produced *via* HTS have no impurities. In contrast, those synthesized by the tube method show NiO segregations. This further highlights the superior capability in synthesizing cathode materials of HTS, particularly for O3 cathodes (Fig. S16, ESI†).

Electrochemical performance

The sodium storage capabilities of HT-NCP@333 and Tu-NCP@333 were evaluated in half cells. Fig. S17 (ESI†) shows the electrochemical behavior of HTS cathodes with different NCP concentrations (1 mol%, 2 mol%, 3 mol%) on NFM333. The 1 mol% NCP-coated cathode has better initial capacity and cycling stability, making it the benchmark to compare HT-NCP@333 and Tu-NCP@333. Fig. 3(a) compares the electrochemical behaviors of the Tu-333 and HT-333 cathode materials, showing similar initial capacities of around 147 mA h g^{-1} across a voltage range of 2.0–4.0 V at the discharge rate of 0.1C. However, the Tu-NCP@333 recorded the lowest capacity at 138 mA h g^{-1}, attributable to the NiO impurities on its surface, which impedes ion transport. The cyclic voltammetry curves (Fig. 3(b) and (c)) further illustrate these performance disparities. The HT-NCP@333 cathodes maintain consistent performance over multiple cycles, indicating stable electrochemical properties. In contrast, the Tu-NCP@333 cathodes exhibited significant performance degradation after the first cycle, which is due to material alterations or irreversible reactions with the electrolyte. Fig. 3(d) illustrates the cycling performance of HT-NCP@333 and Tu-NCP@333. The tests were conducted at a 1C discharge rate and 30 °C, within a voltage range of 2.0–4.0 V. Uncoated materials of both HT-333 and Tu-333 have lower cycling stability. In contrast, coated materials exhibit enhanced stability, with the Tu-NCP@333 sample retaining 52.5% of its capacity after 1000 cycles. In contrast, HT-NCP@333 shows capacity retention of 80% after 1000 cycles, underscoring its significantly enhanced stability. This can be attributed to higher purity and structural integrity. Regarding rate performance (Fig. 3(e)), the HT-NCP@333 cathode maintains consistent capacities across various cycling rates (0.1, 0.5, 1, 2, 5, 10, and 20C), with capacities of 149.1, 137.1, 132.1, 126.3, 115.7, 102.5, and 81.6 mA h g^{-1}, respectively. In comparison, the Tu-NCP@333 cathode exhibits lower discharge capacities at the same rates, with values of 146, 135.2, 130.7, 124.8, 114.3, 99.9, and 69.2 mA h g^{-1}, respectively. These results clearly demonstrate that the surface-modified $NaCaPO_4$ enhances the Na^+ diffusion coefficient and facilitates the kinetics of the cathode reaction in anionic redox reactions, resulting in improved rate performance. Fig. S22(a) (ESI†) displays the low-temperature cycling performance (−25 °C) of two materials. HT-NCP@333 shows a discharge capacity of ∼115 mA h g^{-1} and capacity retention of 83% after 200 cycles, significantly outperforming the Tu-NCP@333. Fig. S22b (ESI†) indicates that at 45 °C, after 270 cycles, HT-NCP@333 retains ∼80% capacity retention, in contrast to Tu-NCP@333 of ∼73%. The superior performance of HT-NCP@333 in extreme conditions is derived from the ultrastable structure. Electrochemical impedance spectroscopy (EIS) shows that the HT-NCP@333 cathode has a smaller increase in impedance over several cycles compared to Tu-NCP@333, indicating better stability and electrochemical interface performance during cycling (Fig. S15, ESI†). The galvanostatic intermittent titration technique (GITT) and cyclic voltammetry (CV) curves at various sweep rates assay were utilized to evaluate the diffusivity of Na^+ in Tu-NCP@333 and HT-NCP@333, as depicted in Fig. 3(f) and Fig. S19 and S20 (ESI†). The diffusion coefficient of Na^+ in HT-NCP@333 ranges from 10^{-9} to 10^{-10} cm^2 s^{-1}, which is one order of magnitude higher than that observed for Tu-NCP@333. These measurements demonstrate that HT-NCP@333 has superior rate and cycling performance due to enhanced structural stability and higher Na-ion diffusion coefficients. XRD patterns show that the O3-type layered material undergoes structural changes after 3 and 7 days of exposure (Fig. S21, ESI†). Materials synthesized by HTS exhibit better air stability compared to those synthesized by tube, especially after 7 days, as demonstrated by smaller degradation peaks of NiO and Na_2CO_3. HT-NCP@333 maintained higher specific capacity with smaller voltage drops, demonstrating superior electrochemical performance (Fig. 3(g)). However, increased polarization and significantly reduced capacity were observed in the Tu-NCP@333, attributed to surface alkaline impurities. These results highlight the superior performance of HT-NCP@333, especially in discharge capacity, loading, cycle life,

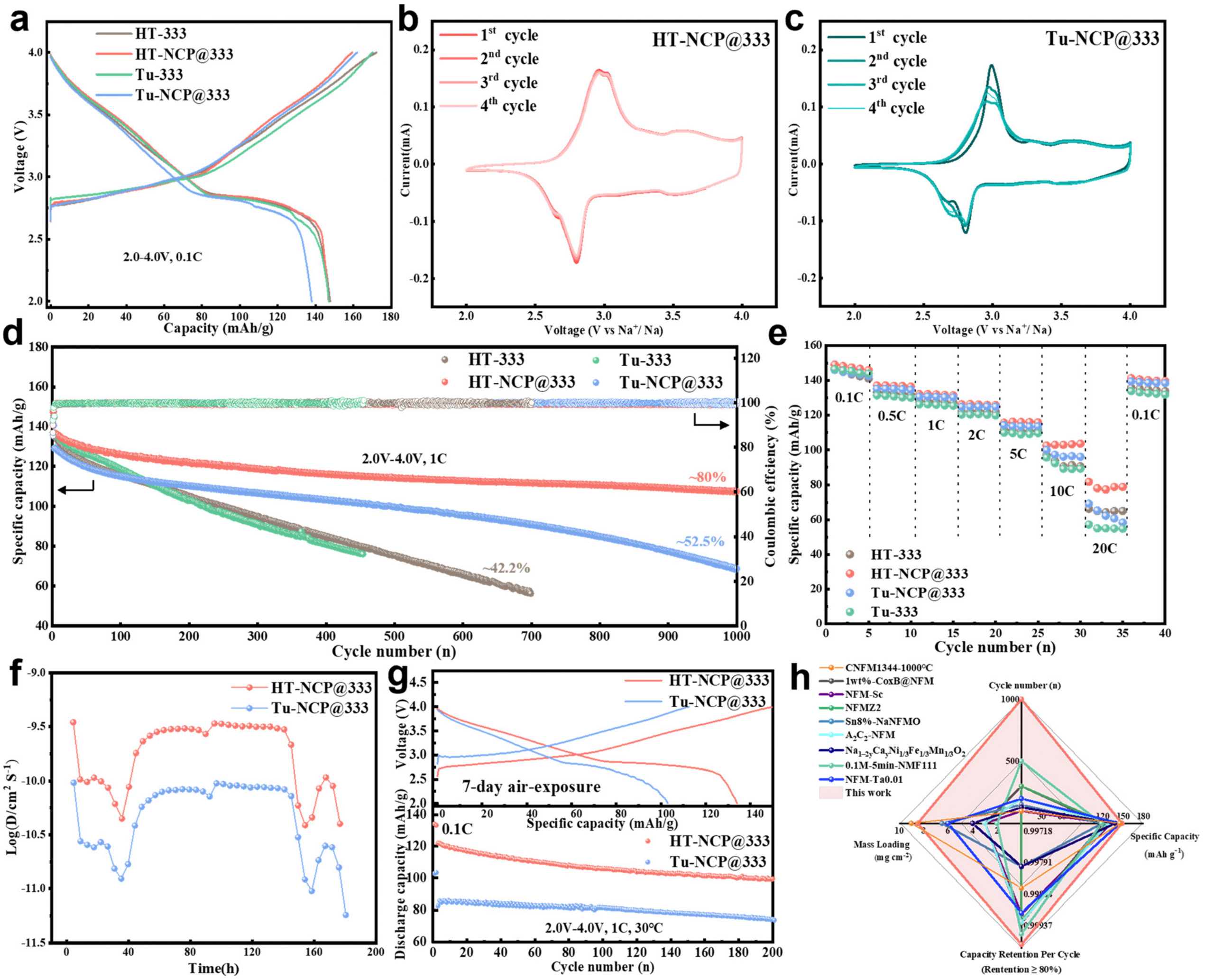

Fig. 3 The electrochemical properties of NFM333 cathodes. (a) Charge–discharge curves of HT-333, HT-NCP@333, Tu-333 and Tu-NCP@333 cathodes at 0.1C (here 1C is defined as 140 mA g^{-1}) during the first cycle in half cells. Initial to fourth cyclic voltammetry (CV) curves of (b) HT-NCP@333 and (c) Tu-NCP@333. (d) Cycling performance of HT-333, HT-NCP@333, Tu-333 and Tu-NCP@333, respectively. (e) Rate performance of HT-333, HT-NCP@333, Tu-333 and Tu-NCP@333, respectively. (f) Calculated Na^+ diffusivity from the galvanostatic intermittent titration technique (GITT) of HT-NCP@333 and Tu-NCP@333, respectively. (g) Initial galvanostatic charge–discharge curves and cycling performance of HT-NCP@333 and Tu-NCP@333 electrodes upon 7 days of air exposure. (h) Comparison of the electrochemical performance of the half-cell using HT-NCP@333 with other NFM333 cathode materials reported in previous research.

and capacity retention, surpassing NFM333 materials reported over the past three years (Fig. 3(h)).[35–43]

Redox mechanism and structural evolution upon electrochemical cycling

The structural evolution of Tu-NCP@333 and HT-NCP@333 during initial charge–discharge cycles was investigated using *in situ* XRD. The initial charging process changes the crystal structure of Tu-NCP@333. Specifically, the (104) peak of the O3 phase shifts to a higher angle and splits into (111), while the (003) peak moves to a lower angle, becoming the (006) peak of Tu-NCP@333. These changes lead to the formation of a monoclinic O′3 phase with a *C*2/*m* space group, resulting from the collective Jahn–Teller distortion involving $Ni^{3+}O_6$ complexes.[44] Both O3 and O′3 phases have rhombohedral structures. This similarity contributes to performance degradation during cycling (Fig. 4(b) and Fig. S23(b), ESI†). In contrast, HT-NCP@333 maintains better structural stability as it does not transit into an O′3 phase. As the charging voltage increases to around 3.9 V, the (003) diffraction peaks of HT-NCP@333 electrodes shift to higher angles and become broader, without significant peak splitting. This is attributed to the formation of an OP2-like stacking structure. An O/P intergrowth phase transition occurs below 4.0 V, which is significantly lower than the documented 4.2 V. This lower voltage threshold helps inhibit lattice and interlayer expansion, thus maintaining structural integrity at higher voltages. However, the Tu-NCP@333 electrodes only undergo a phase transition from O′3 to P3, without an intermediate OP2 phase (Fig. 4(a) and Fig. S23(b), ESI†). Rietveld refinement of *in situ* XRD data reveals the lattice parameters (Fig. 4(c) and (d)). The diffraction peaks of (003) and (006) for HT-NCP@333 and Tu-NCP@333 shift to smaller angles due to

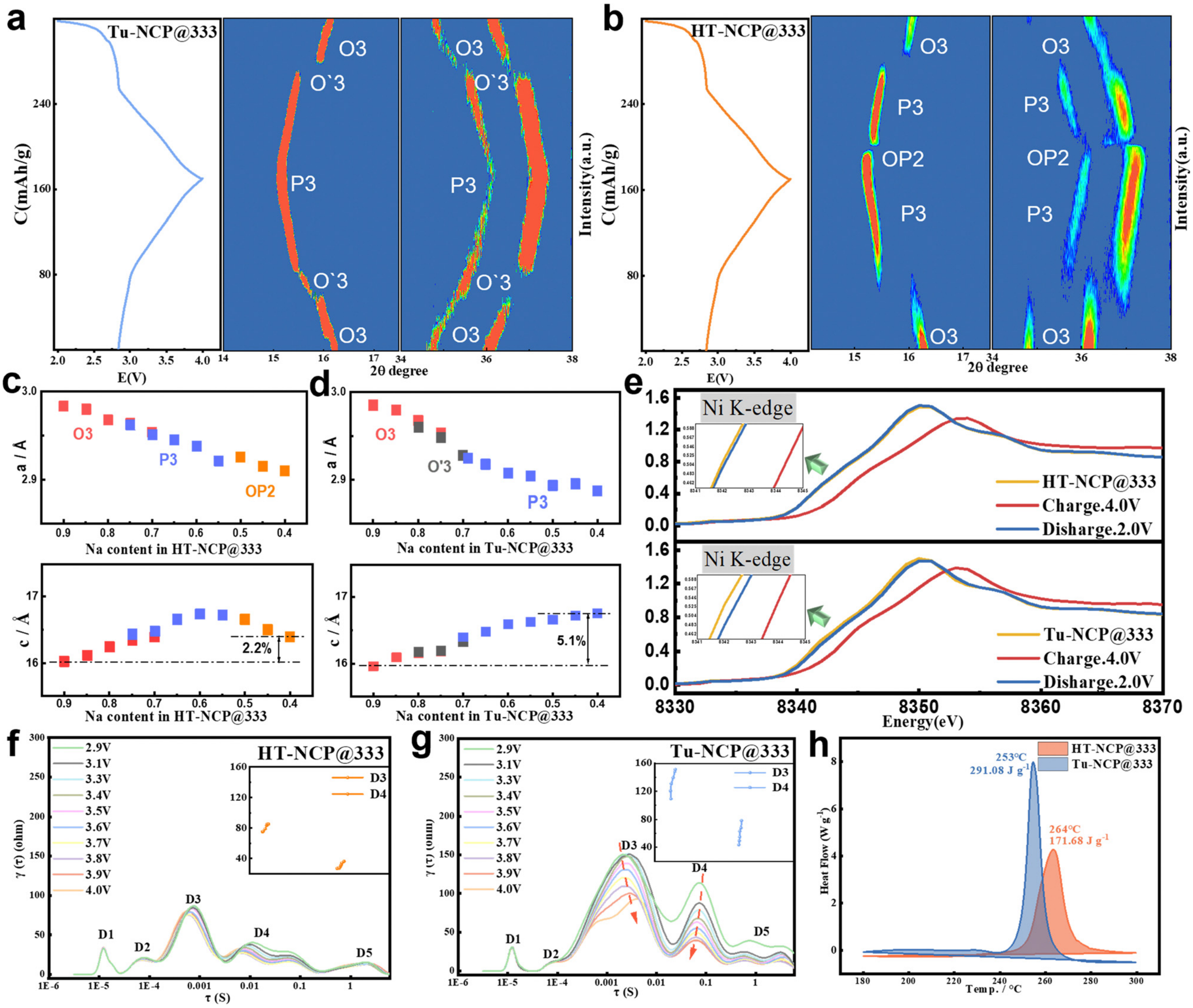

Fig. 4 Structural characterizations and kinetic analysis of the electrochemical behavior for HT-NCP@333 and Tu-NCP@333 electrodes. Initial charge curves, contour maps of *in situ* XRD of (a) HT-NCP@333 and (b) Tu-NCP@333. Evolution of lattice parameters (*a*-axis, *c*-axis) calculated from the *in situ* XRD data of (c) HT-NCP@333 and (d) Tu-NCP@333. (e) X-ray absorption near-edge structure of Ni K edges of HT-NCP@333 and Tu-NCP@333 during the first charge and discharge. *In situ* DRT analysis of (f) HT-NCP@333 and (g) Tu-NCP@333 during charge and discharge processes. (h) DSC curves of HT-NCP@333 and Tu-NCP@333 cathodes charged to 4.0 V at a heating rate of 5 °C min^{-1} after 5 cycles.

the increased *c* lattice parameter derived from expanded Na interlayer spacing. In contrast, the (101) and (012) peaks shift to higher angles due to a reduction in the lattice parameter, attributed to the contraction of the TM–TM bonds. In a fully charged state, HT-NCP@333 exhibits a minimal 2.2% change in *c* lattice parameter compared to its initial state. This highlights the excellent structural stability of HT-NCP@333, which in turn accounts for its excellent capacity retention during extended cycles. These findings indicate that the HT-NCP@333 experiences simpler and more reversible phase transitions during Na$^+$ extraction and insertion. Consequently, this leads to a more stable crystal structure, increased battery capacity, and enhanced cycling stability. X-ray absorption near-edge spectroscopy (XANES) measurements characterized the valence states and coordination of transition metal (TM) ions in HTS and tube cathodes, revealing distinct behaviors during charge and discharge cycles (Fig. 4(e) and Fig. S24, ESI†). Upon charging to 4.0 V, both HT-NCP@333 and Tu-NCP@333 exhibit changes in the nickel valence state from Ni^{2+} to Ni^{4+}. Simultaneously, the HT-NCP@333 shows a more significant increase in energy levels compared to the Tu-NCP@333. This suggests a higher initial capacity for the HT-NCP@333. Notably, after discharging to 2.0 V, the Tu-NCP@333 retains a significant shift from its pristine state, suggesting irreversible changes impacting the stability and cycling life. XPS analysis indicates that HT-NCP@333 consists solely of Ni^{2+}. Conversely, Tu-NCP@333, due to NiO impurities, incorporates a minor fraction of Ni^{3+} within its structure (Fig. 2(h)). These observations align well with XANES data, highlighting a greater concentration of charge-compensating Ni^{2+} in the HT-NCP@333 cathode, which improves its initial specific capacity. The Fe K-edge spectrum shifts to a higher energy level, indicating the oxidation of Fe^{3+}

to Fe^{4+} (Fig. S24, ESI†). Compared to the Tu-NCP@333, the HT-NCP@333 electrode maintains a stable peak intensity and edge position, with only a minor change in the K-edge shape due to alterations in the local Fe environment, emphasizing the high structural reversibility of HT-NCP@333. Fig. S25 (ESI†) shows the extended X-ray absorption fine structure (EXAFS) spectra for nickel and iron, which indicates a reduction in the interatomic distances within the first coordination shell of nickel and a decrease in the Fourier transform amplitude. These changes suggest redox activity in nickel during electrochemical cycling, along with the contraction of TMO_6 octahedra. These findings align well with the reduction in the lattice parameter observed in XANES and the refined XRD in Fig. 4(c). Conversely, the surrounding structure of Fe ions shows no change. This comparative analysis highlights the differences in electrochemical response and stability between the two materials, which is critical for optimizing battery performance and durability. We further utilized *in situ* electrochemical impedance spectroscopy (EIS) to analyze the electrochemical dynamics of tube-NCP@333 and HT-NCP@333 during various phase transitions. Analysis of Nyquist plots during the charging process (Fig. S26(a), ESI†) reveals two characteristic incomplete semicircles. These correspond to the high-frequency impedance of the solid electrolyte interphase (SEI) layer and the low-frequency charge transfer impedance. Additionally, we employed the distribution of relaxation times (DRT) technique to investigate sub-steps in the electrode processes.[45] This method effectively identifies the number, contributions, and characteristic time constants of polarization processes in secondary batteries. As shown in Fig. S28 (ESI†), peak values in the high-frequency region ($\tau = 10^{-5}$ to 10^{-3}) are linked to the particles and their interface with the current collector (D1 and D2). The mid-frequency region ($\tau = 10^{-3}$ to 10) corresponds to the charge transfer process ($D3$ and $D4$). Meanwhile, the low-frequency area ($\tau = 10$ to 10^2) is primarily due to the sodium ion intercalation process ($D5$).[46,47] The peaks in the DRT analysis, alongside their corresponding kinetic processes, are detailed in Table S7 (ESI†). During the charging process, the $D3$ and $D4$ values of the HT-NCP@333 are significantly lower than those of the Tu-NCP@333, indicating more efficient ionic transport at the interface of the HTS (Fig. 4(f) and (g)). The primary difference arises from the uniform coating on the surface of HT-NCP@333 with the plastic NCP, which enables efficient ion transport due to the absence of a rock salt passivation layer. Without this coating, materials show significantly higher impedance during charging. This underscores the vital importance of NCP modification (Fig. S26(b), ESI†). Additionally, corresponding to the *in situ* XRD results, significant changes in the $D3$ and $D4$ values are observed in the Tu-NCP@333

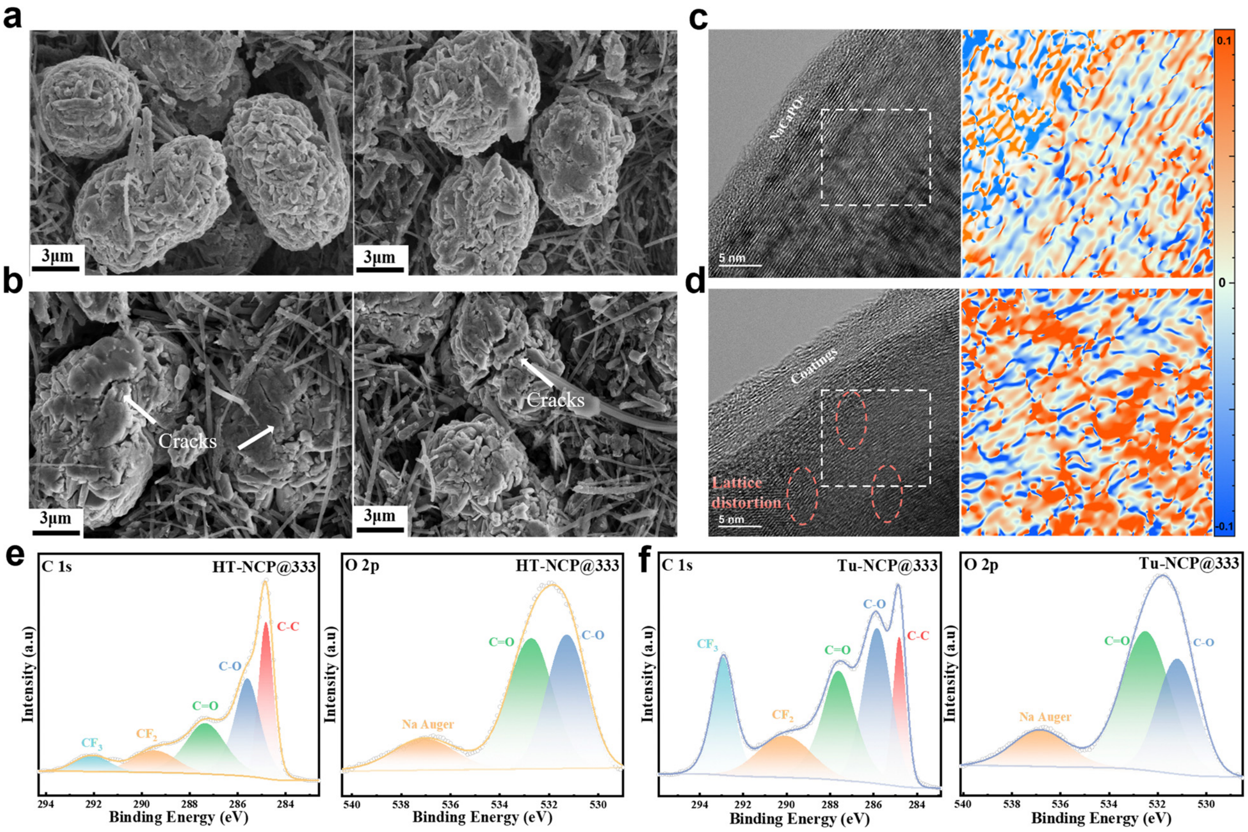

Fig. 5 Evolution of the surface chemistry and structure for the HT-NCP@333 and Tu-NCP@333 electrodes after 500 cycles. SEM images for the (a) HT-NCP@333 and (b) Tu-NCP@333 cathodes after 500 cycles. The TEM image of (c) HT-NCP@333 and (d) Tu-NCP@333 after 500 cycles and corresponding localized strain distribution analysis by GPA (white squares region). XPS analysis of C 1s and O 2p for (e) HT-NCP@333 and (f) Tu-NCP@333 after 500 cycles.

when the voltage reaches 3.3 V, reflecting complex phase transitions within its structure. In contrast, the HTS material exhibits almost no structural changes during the deintercalation of sodium ions, indicating better structural stability. The *in situ* EIS impedance spectra and fitting results are listed in Fig. S26(a) and S27 (ESI†). Fig. 4(h) compares the differential scanning calorimetry (DSC) outcomes for HT-NCP@333 and Tu-NCP@333 after 5 cycles. At 253 °C, HT-NCP@333 exhibits a thermal decomposition peak with an energy release of 171.68 J g^{-1}, which is much lower than the 264 °C peak of Tu-NCP@333. This suggests that HT-NCP@333 decomposes more efficiently with less heat and shows greater thermal stability. This behavior aligns with its performance in high-temperature electrochemical tests.

The structural durability and completeness of the cathode after cycling were performed using SEM, HRTEM and geometric phase analysis (GPA). After 500 cycles at a 1C current density, SEM analyses of HT-NCP@333 and Tu-NCP@333 at half-charge show notable structural changes. The Tu-NCP@333 exhibits significant cracks and surface disruptions (Fig. 5(b) and Fig. S29(b), ESI†). This damage is likely due to the instability of the NiO rock salt phase, leading to microcracks. These cracks and particle fragmentation increase the specific surface area of the materials, which facilitates the rapid formation of new cathode–electrolyte interfaces (CEI).[48] The formation of CEIs depletes sodium ions and increases battery polarization, which contributes to capacity degradation. In contrast, the HT-NCP@333 exhibits minimal cracking (Fig. 5(a) and Fig. S29(a), ESI†). The inner composition of cathodes within cycled cathode materials was observed using transmission electron microscopy (TEM). Due to decomposition during sample preparation and electron beam exposure, the CEI film is not observed. HRTEM images indicate significant lattice distortions and dislocations within the grains of Tu-NCP@333, which is caused by the propagation of microcracks into the material (Fig. 5(d)). In contrast, the HT-NCP@333 maintained a well-preserved crystalline structure post-cycling. The atomic arrangement in HT-NCP@333 remains ordered, without significant lattice distortions or mismatches (Fig. 5(c)). GPA analysis of selected regions also demonstrates that the HT-NCP@333 experienced less and more uniform internal strain. These observations indicate that the HTS method effectively suppresses the formation of surface rock-salt phases, mitigates adverse structural changes during cycling, and enhances cycling stability. Fig. 5(e) and (f) show XPS spectra detailing the surface composition of HT-NCP@333 and Tu-NCP@333 electrodes in the C 1s and O 2p regions. Both electrodes exhibit C=O and C—O groups, resulting from the decomposition of the electrolyte solvent (EC, DEC). The CF_x peaks, including CF_3 and CF_2, are related to $NaPF_6$ and the PVDF binder.[49,50] In comparison, the HT-NCP@333 electrode shows reduced byproduct formation after cycling, indicating a more stable interface and thinner CEI layer. This suggests that its surface can mitigate side reactions with the electrolyte more effectively, facilitating enhanced Na^+ transport.

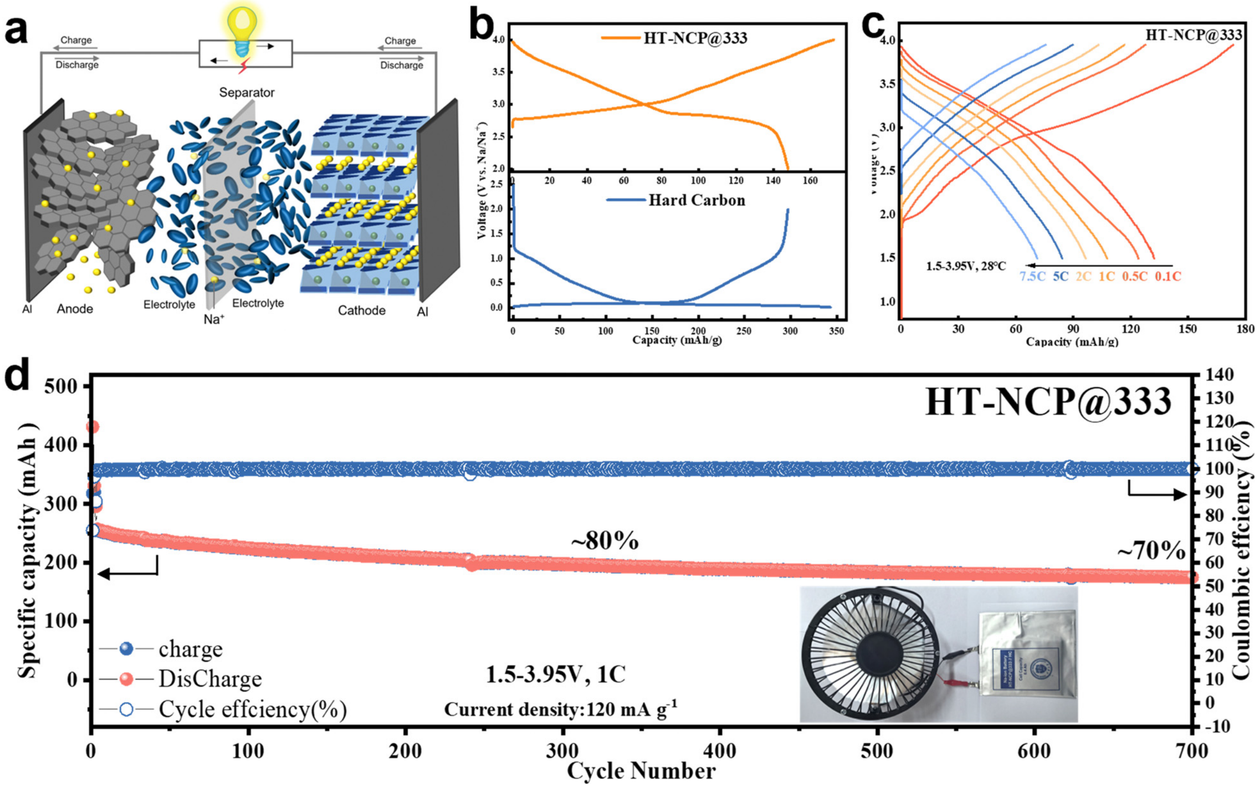

Fig. 6 (a) Schematic of the HT-NCP@333//HC pouch full cell. (b) Initial charge–discharge profiles of HT-NCP@333 and hard carbon (HC) with a capacity ratio of 1.1 : 1 of electrodes (negative and positive). (c) Charge–discharge profile at 0.1C, 0.5C, 1C, 2C, 5C and 7.5C of the HT-NCP@333//HC pouch cell. (d) Cycling performance of HT-NCP@333//HC at a current rate of 1C.

These findings support the idea that HTS treatment stabilizes the electrode surface more effectively, leading to improved performance.

Modulation toward practical applications

The schematic of the sodium-ion pouch cell is depicted in Fig. 6(a). To evaluate the application potential of HTS and HT-NCP@333 materials, pouch cells were constructed using HT-NCP@333 as the cathode and hard carbon (HC) as the anode. At a current density of 15 mA g^{-1}, the reversible specific capacity of the cathode and anode is recorded at 147.3 mA h g^{-1} and 294 mA h g^{-1}, respectively (Fig. 6(b)). This resulted in a capacity ratio of 1.1 : 1 between the negative and positive electrodes. The HT-NCP@333//HC pouch cell exhibits a capacity of 0.3 Ah and an energy density of 115 W h kg^{-1}, based on total weight of the cell (Table S8, ESI†). During rate cycling tests at 1C, the cell delivered a capacity of approximately 108 mA h g^{-1}, referring to the cathode active mass, and maintained a 66% capacity retention when the rate is increased to 7.5C (Fig. 6(c)), indicating exceptional rate performance. Additionally, after 700 cycles at 1C, the cell preserves ∼70% of its initial capacity, with all coulombic efficiency (CE) surpassing 99.9%, as illustrated in Fig. 6(d). After 700 cycles, the pouch cell can keep the fan running. These results underscore the significant practical potential of HT-NCP@333. The enhanced safety and efficacy of HTS synthetic materials in pouch cells underscores their extensive potential for application in sodium-ion batteries (SIBs).

Conclusions

In this study, we introduced an innovative high-temperature shock (HTS) technique to synthesize the uniformly coated HT-NCP@333 material. The HTS process involves rapid heating, cooling, and a brief dwelling period, which facilitates homogeneous material distribution and uniform coating. This uniformity effectively prevents nickel segregation, as confirmed by HAADF-STEM and synchrotron radiation XRD analyses. The HTS technique ensures crack-free morphology of the HT-NCP@333, which refrains transition metal migration, avoids performance degradation during cycling, and significantly enhances its electrochemical performance. Specifically, the HT-NCP@333 retains 80% capacity after 1000 cycles at a 1C rate, which dramatically enhanced compared to 52.5% of the Tu-NCP@333. Additionally, HT-NCP@333//HC pouch cells maintain over 70% capacity after 700 cycles. The HTS method shows excellent scalability and commercialization potential for the sustainable development of sodium-ion battery technology.

Author contributions

C. Y. N. planned and supervised the project. L. Z. K. conducted material synthesis, characterization, and analysis. H. P. F. and Z. J. F. acquired and analyzed STEM data. L. Z. K. wrote the manuscript, and all authors contributed to the discussion and provided feedback on the manuscript.

Data availability

All data relevant to this article are available within the main text and the ESI.† The raw data from this study can be obtained from the corresponding author upon reasonable request.

Conflicts of interest

The authors declare no competing interests.

Acknowledgements

The authors thank the staff of beamline BL13SSW at Shanghai Synchrotron Radiation Facility for experimental support. The authors acknowledge the support from the National Natural Science Foundation of China (No. 92372107, 52403307, 52171219 and U22A20119).

References

1 A. Rudola, R. Sayers, C. J. Wright and J. Barker, *Nat. Energy*, 2023, **8**, 215–218.

2 E. Gabriel, C. Ma, K. Graff, A. Conrado, D. Hou and H. Xiong, *eScience*, 2023, **3**, 100139.

3 X. Rong, D. Xiao, Q. Li, Y. Niu, F. Ding, X. Hou, Q. Wang, J. Xu, C. Zhao, D. Zhou, R. Xiao, X. Yu, W. Yin, L. Gu, H. Li, X. Huang, L. Chen and Y.-S. Hu, *eScience*, 2023, **3**, 100159.

4 N. Yabuuchi, M. Kajiyama, J. Iwatate, H. Nishikawa, S. Hitomi, R. Okuyama, R. Usui, Y. Yamada and S. Komaba, *Nat. Mater.*, 2012, **11**, 512–517.

5 Y. Li, Q. Zhou, S. Weng, F. Ding, X. Qi, J. Lu, Y. Li, X. Zhang, X. Rong, Y. Lu, X. Wang, R. Xiao, H. Li, X. Huang, L. Chen and Y.-S. Hu, *Nat. Energy*, 2022, **7**, 511–519.

6 Z. Guo, G. Qian, C. Wang, G. Zhang, R. Yin, W.-D. Liu, R. Liu and Y. Chen, *Prog. Nat. Sci.: Mater. Int.*, 2023, **33**, 1–7.

7 Z.-F. Ma, H. Wang, G.-L. Xu, J. Wang, H. Sheng, Z. Chen, Y. Ren, C.-J. Sun, J. Wen, J. Wang, D. Miller, J. Lu, K. Amine and Z.-F. Ma, *Adv. Energy Mater.*, 2016, **6**, 1601306.

8 C. Liu, K. Chen, H. Xiong, A. Zhao, H. Zhang, Q. Li, X. Ai, H. Yang, Y. Fang and Y. Cao, *eScience*, 2024, **4**, 100186.

9 X.-Q. Xu, J.-Y. Chen, Y. Jiang, B. Xu, X.-L. Li, C.-Y. Ouyang and J.-X. Zheng, *J. Am. Chem. Soc.*, 2024, **146**, 22374–22386.

10 A. Yang, K. Yao, M. Schaller, E. Dashjav, H. Li, S. Zhao, Q. Zhang, M. Etter, X. Shen, H. Song, Q. Lu, R. Ye, I. Moudrakovski, Q. Pang, S. Indris, X. Wang, Q. Ma, F. Tietz, J. Chen and O. Guillon, *eScience*, 2023, **3**, 100175.

11 M. Gu, I. Belharouak, A. Genc, Z. Wang, D. Wang, K. Amine, F. Gao, G. Zhou, S. Thevuthasan, D. R. Baer, J.-G. Zhang, N. D. Browning, J. Liu and C. Wang, *Nano Lett.*, 2012, **12**, 5186–5191.

12 P.-F. Wang, H.-R. Yao, X.-Y. Liu, J.-N. Zhang, L. Gu, X.-Q. Yu, Y.-X. Yin and Y.-G. Guo, *Adv. Mater.*, 2017, **29**, 1700210.

13 R. Fielden and M. N. Obrovac, *J. Electrochem. Soc.*, 2015, **162**, A453.

14 C. Delmas, Y. Borthomieu, C. Faure, A. Delahaye and M. Figlarz, *Solid State Ionics*, 1989, **32–33**, 104–111.

15 H. Liu, Z. Xie, W. Qu, E. Dy, S. Niketic, S. Brueckner, K. Tsay, E. Fuller, C. Bock, N. Zaker and G. A. Botton, *Small*, 2022, **18**, 2200627.

16 M. Cai, Y. Dong, M. Xie, W. Dong, C. Dong, P. Dai, H. Zhang, X. Wang, X. Sun, S. Zhang, M. Yoon, H. Xu, Y. Ge, J. Li and F. Huang, *Nat. Energy*, 2023, **8**, 159–168.

17 S. Schweidler, T. Brezesinski and B. Breitung, *Nat. Energy*, 2024, **9**, 240–241.

18 D. Lei, Y.-B. He, H. Huang, Y. Yuan, G. Zhong, Q. Zhao, X. Hao, D. Zhang, C. Lai, S. Zhang, J. Ma, Y. Wei, Q. Yu, W. Lv, Y. Yu, B. Li, Q.-H. Yang, Y. Yang, J. Lu and F. Kang, *Nat. Commun.*, 2019, **10**, 4244.

19 E. A. Cheung, H. Nguyen, H. Tang, A. P. J. Stampfl, M. Avdeev, Y. S. Meng, N. Sharma and N. R. de Souza, *J. Am. Chem. Soc.*, 2021, **143**, 17079–17089.

20 H. Wang, F. Ding, Y. Wang, Z. Han, R. Dang, H. Yu, Y. Yang, Z. Chen, Y. Li, F. Xie, S. Zhang, H. Zhang, D. Song, X. Rong, L. Zhang, J. Xu, W. Yin, Y. Lu, R. Xiao, D. Su, L. Chen and Y.-S. Hu, *ACS Energy Lett.*, 2023, **8**, 1434–1444.

21 W. Xu, R. Dang, L. Zhou, Y. Yang, T. Lin, Q. Guo, F. Xie, Z. Hu, F. Ding, Y. Liu, Y. Liu, H. Mao, J. Hong, Z. Zuo, X. Wang, R. Yang, X. Jin, X. Hou, Y. Lu, X. Rong, N. Xu and Y.-S. Hu, *Adv. Mater.*, 2023, **35**, 2301314.

22 J. Dai, Z. He, X. Li, G. Yan, H. Duan, G. Li, Z. Wang, H. Guo, W. Peng and J. Wang, *Chin. Chem. Lett.*, 2024, **28**, 110063.

23 A. J. Hooper, P. Mcgeehin, K. T. Harrison and B. C. Tofield, *J. Solid State Chem.*, 1978, **24**, 265–275.

24 W. Zhu, J. Zhang, J. Luo, C. Zeng, H. Su, J. Zhang, R. Liu, E. Hu, Y. Liu, W.-D. Liu, Y. Chen, W. Hu and Y. Xu, *Adv. Mater.*, 2023, **35**, 2208974.

25 Z. Guo, H. Jiang, X. Sun, X. Li, Z. Liu, J. Zhang, J. Luo, J. Zhang, X.-S. Tao, J. Ding, X. Han, R. Liu, Y. Chen and W. Hu, *Adv. Energy Mater.*, 2024, **14**, 2302484.

26 J. Luo, J. Zhang, Z. Guo, Z. Liu, C. Wang, H. Jiang, J. Zhang, L. Fan, H. Zhu, Y. Xu, R. Liu, J. Ding, Y. Chen and W. Hu, *Adv. Mater.*, 2024, **36**, 2405956.

27 H. Jiang, C. Zeng, W. Zhu, J. Luo, Z. Liu, J. Zhang, R. Liu, Y. Xu, Y. Chen and W. Hu, *Nano Res.*, 2024, **17**, 2671–2677.

28 Z. Liu, J. Zhang, J. Luo, Z. Guo, H. Jiang, Z. Li, Y. Liu, Z. Song, R. Liu, W.-D. Liu, W. Hu and Y. Chen, *Nano-Micro Lett.*, 2024, **16**, 210.

29 R. Yin, Z. Guo, R. Liu and X.-S. Tao, *Chin. Chem. Lett.*, 2025, **36**, 109643.

30 L. Sun, Y. Xie, X.-Z. Liao, H. Wang, G. Tan, Z. Chen, Y. Ren, J. Gim, W. Tang, Y.-S. He, K. Amine and Z.-F. Ma, *Small*, 2018, **14**, 1704523.

31 F. Ding, H. Wang, Q. Zhang, L. Zheng, H. Guo, P. Yu, N. Zhang, Q. Guo, F. Xie, R. Dang, X. Rong, Y. Lu, R. Xiao, L. Chen and Y.-S. Hu, *J. Am. Chem. Soc.*, 2023, **145**, 13592–13602.

32 W. Zuo, J. Gim, T. Li, D. Hou, Y. Gao, S. Zhou, C. Zhao, X. Jia, Z. Yang, Y. Liu, W. Xu, X. Xiao, G.-L. Xu and K. Amine, *Nat. Nanotechnol.*, 2024, **19**, 1644–1653.

33 R. Lin, R. Zhang, C. Wang, X.-Q. Yang and H. L. Xin, *Sci. Rep.*, 2021, **11**, 5386.

34 S.-Q. Lu, Q. Zhang, F. Meng, Y.-N. Liu, J. Mao, S. Guo, M.-Y. Qi, Y.-S. Xu, Y. Qiao, S.-D. Zhang, K. Jiang, L. Gu, Y. Xia, S. Chen, G. Chen, A.-M. Cao and L.-J. Wan, *J. Am. Chem. Soc.*, 2023, **145**, 7397–7407.

35 Y. Yang, Z. Wang, C. Du, B. Wang, X. Li, S. Wu, X. Li, X. Zhang, X. Wang, Y. Niu, F. Ding, X. Rong, Y. Lu, N. Zhang, J. Xu, R. Xiao, Q. Zhang, X. Wang, W. Yin, J. Zhao, L. Chen, J. Huang and Y.-S. Hu, *Science*, 2024, **385**, 744–752.

36 S. Feng, Y. Lu, X. Lu, H. Chen, X. Wu, M. Wu, F. Xu and Z. Wen, *Adv. Energy Mater.*, 2024, **14**, 2303773.

37 N. Hong, J. Li, H. Wang, X. Hu, B. Zhao, F. Hua, Y. Mei, J. Huang, B. Zhang, W. Jian, J. Gao, Y. Tian, X. Shi, W. Deng, G. Zou, H. Hou, Z. Hu, Z. Long and X. Ji, *Adv. Funct. Mater.*, 2024, **34**, 2402398.

38 C. Jiang, Y. Wang, Y. Xin, X. Ding, S. Liu, Y. Pang, B. Chen, Y. Wang, L. Liu, F. Wu and H. Gao, *Carbon Neutralization*, 2024, **3**, 233–244.

39 T. Song, L. Chen, D. Gastol, B. Dong, J. F. Marco, F. Berry, P. Slater, D. Reed and E. Kendrick, *Chem. Mater.*, 2022, **34**, 4153–4165.

40 L. Zhang, J. Deshmukh, H. Hijazi, Z. Ye, M. B. Johnson, A. George, J. R. Dahn and M. Metzger, *J. Electrochem. Soc.*, 2023, **170**, 070514.

41 Y. Hao, Y. Xia, W. Liu, G. Sun, L. Feng, X. Zhou, S. Iqbal, Z. Tian, Z. Zhang, Y. Li, X. Zhang and Y. Jiang, *Adv. Sci.*, 2024, **11**, 2401514.

42 W. Wang, Y. Sun, P. Wen, Y. Zhou and D. Zhang, *J. Energy Storage*, 2024, **79**, 110177.

43 G. Sun, Y. Hao, L. Feng, X. Zhou, Z. Tian, Z. Zhang, X. Zhang and Y. Jiang, *Small*, 2024, **20**, 2404593.

44 F. Ding, Q. Meng, P. Yu, H. Wang, Y. Niu, Y. Li, Y. Yang, X. Rong, X. Liu, Y. Lu, L. Chen and Y.-S. Hu, *Adv. Funct. Mater.*, 2021, **31**, 2101475.

45 T. H. Wan, M. Saccoccio, C. Chen and F. Ciucci, *Electrochim. Acta*, 2015, **184**, 483–499.

46 Y. Lu, C.-Z. Zhao, J.-Q. Huang and Q. Zhang, *Joule*, 2022, **6**, 1172–1198.

47 P. Huang, Z. Li, L. Chen, Y. Li, Z. Liu, J. Zhang, J. Luo, W. Zhang, W.-D. Liu, X. Zhang, R. Zhu and Y. Chen, *ACS Nano*, 2024, **18**, 18344–18354.

48 R. Wang, Y. Fan, J. Wang, Y. Li, X. Li, F. Jin and X. Hu, *Prog. Nat. Sci.: Mater. Int.*, 2024, **34**, 1281–1294.

49 Y. Yang, W. Yang, H. Yang and H. Zhou, *eScience*, 2023, **3**, 100170.

50 J. Alvarado, C. Ma, S. Wang, K. Nguyen, M. Kodur and Y. S. Meng, *ACS Appl. Mater. Interfaces*, 2017, **9**, 26518–26530.